Structural integrity of DEMO divertor target assessed by neutron tomography

Triestino Minniti [*],[a], Frank Schoofs [a], Llion Marc Evans [b],[a], Winfried Kockelmann [c], Jeong-Ha You [d], Heather Lewtas [a]

[a] *UKAEA - United Kingdom Atomic Energy Authority, Culham Science Centre, Abingdon, OX14 3DB, United Kingdom*
[b] *College of Engineering, Swansea University, Bay Campus, Swansea, SA1 8EN, United Kingdom*
[c] *STFC, Rutherford Appleton Laboratory, ISIS Facility, Harwell, OX11 0QX, United Kingdom*
[d] *Max Planck Institute for Plasma Physics, Boltzmann Str. 2, Garching 85748, Germany*

A R T I C L E   I N F O

A B S T R A C T

The divertor target plates are the most exposed in-vessel components to high heat flux loads in a fusion reactor due to a combination of plasma bombardment, radiation and nuclear heating. Reliable exhaust systems of such a huge thermal power required a robust and durable divertor target with a sufficiently large heat removal capability and lifetime. In this context, it is pivotal to develop non-destructive evaluation methods to assess the structural integrity of this component that, if compromised could reduced its lifetime. In this work we have demonstrated for the first time the feasibility of using neutron tomography to detect volumetric defects within DEMO divertor mock-ups with a spatial resolution of the order of hundreds of micrometers. Neutron tomography is applicable for studying complex structures, often manufactured from exotic materials which are not favourable for conventional non-destructive evaluation methods. This technique could be effectively used during research and development cycles of fusion component design or for quality assurance during manufacturing.

1. Introduction

Plasma-facing components (PFCs) in a magnetic confinement nuclear fusion reactor are exposed to high heat flux (HHF) loads due to a combination of plasma bombardment, radiation and nuclear heating by neutron irradiation [1]. In addition, neutron irradiation produces defects and damage in plasma-facing materials and pulsed operation causes fatigue due to cyclic thermal stress variation [2,3]. Such issues were recently highlighted in the European roadmap for nuclear fusion as one of the ultimate challenges in view of the design of the nuclear fusion demonstration power plant DEMO [4]. In this context, the paramount engineering challenge is to develop robust and durable PFCs with a sufficiently large heat removal capability and longevity. Since 2014 in the framework of the EUROfusion Consortium, integrated research and development (R&D) efforts have been performed in the work package "Divertor" (WPDIV) where one of the major missions is to deliver a feasible design concept(s) and applicable technology solutions for the divertor target PFCs of DEMO [2]. The most developed divertor PFC consists of an array of rectangular monoblocks of tungsten with a

cooling pipe as heat sink in the middle.

This tungsten monoblock design concept (Fig. 1) was inherited from the ITER divertor target design and it is comprised of tungsten armour blocks threaded onto a CuCrZr cooling pipe separated by a copper interlayer.

In the case of ITER and DEMO reactors, the peak surface heat flux is expected to reach up to 10 MWm^{-2} during normal operation and 20 MWm^{-2} during low transient events like loss of plasma detachment. Therefore, it is vital that PFCs employed in the divertor must maintain structural integrity under HHF fatigue loads and demonstrate reliable HHF performance. This is true in general for any PFC employed in magnetic confinement nuclear fusion reactors. Loss of structural integrity may lead to structural as well as a functional failure of the component. Hence, reliable non-destructive evaluation (NDE) techniques need to be developed and included in any step of the R&D as well as in the subsequent qualification phase of any PFCs used in a nuclear fusion reactor. Nowadays, there are many NDE techniques suitable for the quality evaluation of PFCs [5]. Among them, ultrasonic testing (UT) technique is currently one of the most widely used tools for the
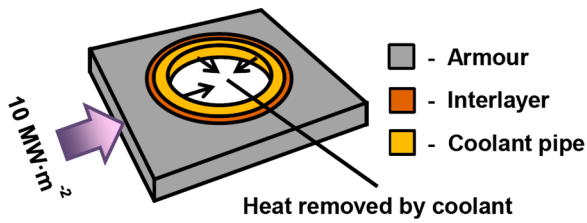

Fig. 1. DEMO tungsten monoblock type design concept.

Fig. 2. Photograph of the phase 2 thermal break mock-ups specimens for the DEMO divertor target. From left to the right: as manufactured (CCFE11), with a single cycle at 25 MWm^{-2} plus 100 cycles at 10 MWm^{-2} (CCFE9), and before HHF testing (CCFE10).
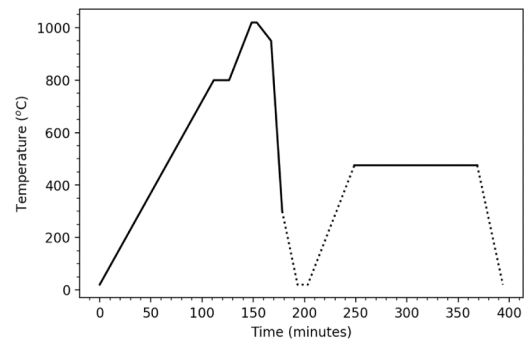

Fig. 3. A single brazing and heat treatment procedure used for fabrication of Phase 2 mock-ups.

2. Sample manufacturing

For this study three sample types of 2nd phase thermal break mock-ups [2,11–14] of the DEMO divertor target design were used: as manufactured (labelled as CCFE11), with a single cycle at 25 MWm^{-2} plus 100 cycles at 10 MWm^{-2} (labelled as CCFE9) performed at the IPP test facility GLADIS [15], and before HHF testing (labelled as CCFE10) as shown in Fig. 2 from left to right.

They were produced by machining tungsten (W) to size and casting oxygen-free high conductivity (OFHC) copper into the bore of the block. The OFHC copper was left 1 mm proud of the W block to allow subsequent thermal break features to be machined into the interlayer. The blocks together with casting were provided by ALMT (Japan). Thermal break features were wire eroded in the interlayer. Parts were precisely bored to match the outer diameter 15.00±0.01mm CuCrZr alloy pipe. The pipes were machined from a solid block of CuCrZr (0.5–1.2% Cr, 0.02-0.07% Zr, rest Cu). Before assembly, the machined CuCrZr pipes were subjected to full brazing/heat treatment cycle and the resulting surface oxide and impurity layer was mechanically removed. All parts were cleaned and assembled along with braze alloy foil (50%Cu/50% Au). The pipe and monoblock assemblies were positioned in bespoke braze tooling which supports the parts and ensures alignment during the brazing procedure.

Brazing was carried out in a vacuum furnace following a single braze/hardening procedure shown in Fig. 3.

In order to achieve good wetting properties, assemblies were heated to 1020°C at 1.8·10^{-5} mbar vacuum. The parts were cooled to 950°C to solidify the braze before a nitrogen gas quench. The quench was carried out by purging nitrogen gas to prevent formation of precipitates and to keep the CuCrZr alloy in a solution annealed state. After the quench, the parts were vacuum aged at 480°C for 2 h to achieve the required hardness.

3. Methodology

Neutron radiography (NR) and tomography (NT) are versatile non-destructive evaluation techniques applied nowadays to a range of material science areas, among them engineering science [16–18]. The structures, orientations of features and materials properties can be inspected inside bulky components given the good penetration of neutrons across different metals. This is particularly true for objects made with very dense materials like tungsten where the well known x-ray imaging technique cannot be applicable due to the lack of transmission of the beam [10]. In this respect, NR and NT are valuable imaging techniques to non-destructively inspect and qualify PFCs. Like any radiographic method (either x-ray or neutron), the resulting image of the object is obtained by counting with a position sensitive detector the fraction of the initial intensity of the beam transmitted through each point in the object. Therefore, any defect within a specimen is translated into a variation of the intensity of the beam after the object. The
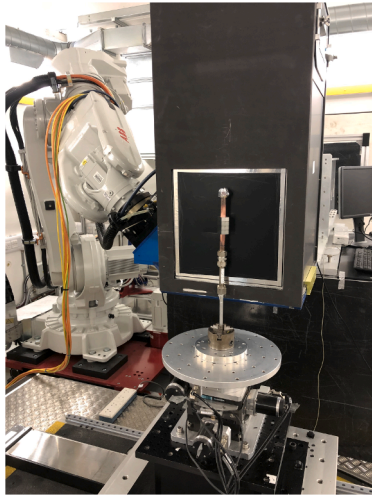
inspection of metal/metal joints as demonstrated by several results [6–9] that are making use of C-scan UT for monoblock Cu-W joints. Despite the common use of ultrasonic scanning in providing a relatively quick verification of PFCs, such technique suffers its inability to distinguish between voids and inclusions as it only measures the changes in acoustic signal from a baseline value. Furthermore, the possible use of complex geometries and/or composite fibers in future generation designs of PFCs will make the detection of component defects by UT-based measurements more difficult.

The choice of alternative non-destructive techniques suitable for the quality evaluation of PFCs is not an easy task due to the presence of tungsten that prevents the use of X-ray imaging techniques commonly employed in aerospace industries. As such, we have identified in neutron tomography an ideal candidate technique capable of providing three-dimensional reconstructions of divertor PFCs [10] and able to detect volumetric defects within the bulk of the scanned component with a spatial resolution of the order of tens of micrometers. In this work we successfully demonstrated that neutron tomography could be used for non-destructive evaluation of volumetric defects in 2nd phase thermal break DEMO divertor mock-ups before and after HHF cycling tests.

Fig. 4. Neutron tomography setup at the IMAT beamline, neutron spallation source, Rutherford Appleton Laboratory, United Kingdom.

mathematical formulation of this concept constitutes the essence of the Beer-Lambert law

$$I_T(x,y,z) = I_0(x,y,z)e^{-\int_{path} \mu_T(x,y,z)ds} \quad (1)$$

where I_0 and I_T are the intensity of the incoming and outgoing beam respectively, and μ_T is the linear attenuation coefficient $\mu_T(x,y,z) = \mu_a(x, y, z) + \mu_s(x, y, z)$, sum of the absorption (μ_a) and scattering (μ_s) coefficients, usually expressed in cm^{-1}. It is worth noting that NR provides a map of the attenuation of the neutron beam brought by the sample and line-integrated along the path length as clearly seen by the exponential part of Eq. (1). However, in a tomography scan one collects multiple radiographies (projections) for distinct angular orientations. From the tomographic scan, one obtains three-dimensional spatially resolved images (i.e. volumetric data), which generally display the attenuation coefficient distribution in the sample volume. This procedure makes use of different reconstruction algorithms, such as filtered back projection (FBP) or iterative based algorithms [19].

3.1. Data acquisition

Neutron images of the three specimens were acquired at the IMAT beamline [20–23], ISIS neutron spallation source, Rutherford Appleton Laboratory, United Kingdom. Each sample was fixed on the rotating

platform using an aluminium tube that was inserted and fixed directly in the CuCrZr pipe, placed at the distance L = 10 m from the beam aperture (pinhole) and at the distance d = 25 mm from the neutron screen scintillator, as shown in Fig. 4.

The selected diameter of the beam aperture was D = 40 mm that defines an L/D ratio of 250, ensuring a neutron flux of $5.9 \cdot 10^6$ n $cm^{-2}s^{-1}$ [22] and a geometric unsharpness of the sample at the image plane of about 100 μm. The detection system consisted of a 16-bit sCMOS camera (ZYLA 4.2 Plus) with 2048 × 2048 pixels coupled with optical lenses and a $^6LiF/ZnS$ based scintillator with thickness of 200 μm. A 50 mm lens with numerical aperture f = 1.2 was employed, assuring a field-of-view (FOV) of 211 x 211 mm^2 and a resulting pixel size of 103 μm. A tomogram for each specimen was collected by performing a uniformly spaced angular scan of 577 projections in the range [0°,360°). The exposure time for each projection was 30 s, which is the maximum exposure time per projection allowed by the camera system. Additionally, a stack of 10 flat field and 10 dark field images were taken as well before and after each tomographic scan for normalization purposes.

3.2. Data processing, CT reconstruction and quantitative evaluation of the image quality

Pre-processing, reconstruction and quantitative evaluation of the image quality were performed using the NeuTomPy toolbox [24] software, whereas the volume rendering and segmentation steps were addressed using Avizo [25]. Quantification and least-squares fitting analyses were computed using the scientific framework for data processing ROOT [26] developed at CERN and the ImageJ software [27].

The acquired datasets with 577 projections all satisfied the sampling theorem [19]. The normalization of the data was performed by using the log-transformation, the flat fielding and the dark subtraction procedure with the correction of the neutron dose [28]. The dose correction applied ensured that all the measured projections received the same amount of incoming neutrons, considering the stability of the neutron beam flux, which is rarely constant at neutron spallation source. The normalization was performed on the data by using the formula:

$$p = -log\left(\frac{D_{flat}}{D} \cdot \frac{I - I_{dark}}{I_{flat} - I_{dark}}\right) \quad (2)$$

where I is the raw projection image, I_{dark} and I_{flat} are the mean of the dark field and flat field images, respectively, while D and D_{flat} are the median computed within a region of interest (ROI) free of sample in the projections and flat images, respectively. Spot filtering (bad camera pixels or direct interaction of gamma rays with the CMOS sensor) were removed from the normalized projections by means of the outlier
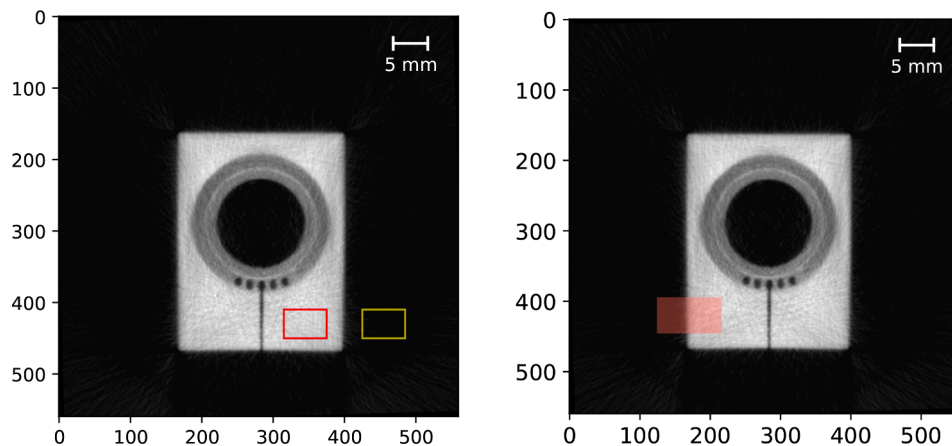

Fig. 5. (Left panel) The signal area (red rectangle) and the background area (yellow rectangle) used for the computation of the CNR. (Right panel) Region of interest containing 20 line profiles used for evaluating the edge quality of the reconstruction. (For interpretation of the references to colour in this figure legend, the reader is referred to the web version of this article.)
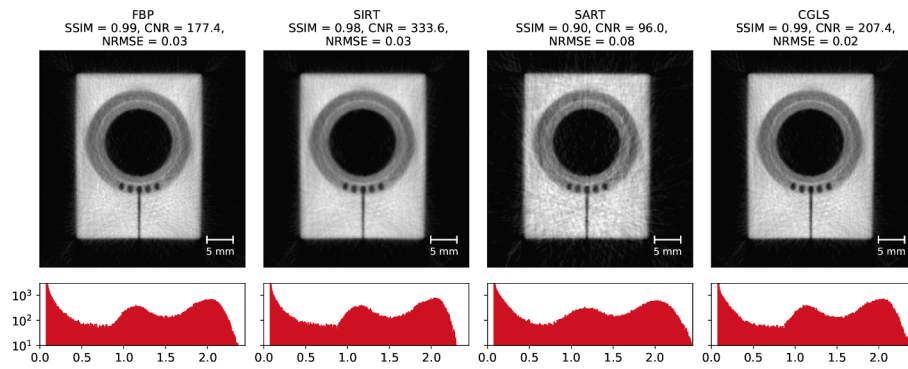
Fig. 6. Comparison of a reconstructed slice for the CCFE11 mock-up carried out with FBP, SIRT, SART, and CGLS reconstruction algorithms considered in this study. Below each image, the grey value histogram is represented in the range [0, 2.45] cm^{-1}.

removal filter implemented in the NeuTomPy toolbox. Ring artefacts, due to defects on the scintillator screen or on the detector, were suppressed by means of a filter based on combined wavelet and Fourier analysis [29]. The CT reconstruction algorithms considered in this study are: Filtered Back Projection (FBP) [19], Simultaneous Iterative Reconstruction Technique (SIRT) [30], Simultaneous Algebraic Reconstruction Technique (SART) [31] and Conjugate Gradient Least Squares (CGLS) [32]. The quality of the CT images reconstructed with the aforementioned algorithms were quantitatively addressed in terms of full-reference and no-reference image quality indexes [33]. In this work, we regarded as the reference image the reconstructed slice obtained by the SIRT method with 800 iterations. In particular, we have made use of the contrast to noise ratio (CNR) index, the structural similarity index (SSIM), and the normalized root mean square error (NRMSE) as previously shown in other works [22,34,35]. It should be noted that higher SSIM and lower NRMSE indicate superior image quality, whereas higher CNR suggests a better signal value with respect to the background levels. The ROIs selected in the reconstructed slice of the CCFE11 mock-up and required to quantify the CNR is depicted in the left panel of Fig. 5.

We considered a region within the Tungsten material (rectangle in red) as a signal, and an area outside the sample was taken as background (rectangle in yellow). In order to assess the edge quality [33], 20 line profiles traced across the Tungsten monoblock edge and contained in the ROI shown in the right panel of Fig. 5 were averaged and the resulting profile, so called the "edge spread function" (ESF), was fitted with a generic sigmoid function [34]:

$$f(x) = \frac{p_0}{2}\{Erf[p_1(x - p_2)] + 1\} + p_3 \tag{3}$$

where p_0, p_1, p_2 and p_3 are fitting parameters and Erf(x) is the Gauss error function defined as:

$$Erf(x) = \frac{2}{\sqrt{\pi}}\int_0^x e^{-t^2}\,dt. \tag{4}$$

The fitting function was then differentiated and the obtained Gaussian has a standard deviation:

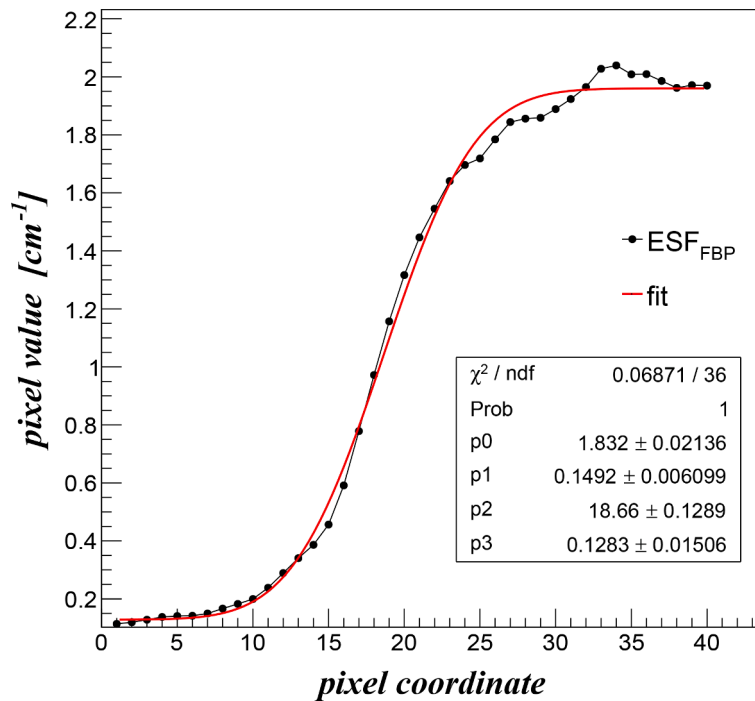$$\sigma = \frac{1}{\sqrt{2}p_1} \tag{5}$$

Fig. 7. Edge quality measurement using the average line profile (black dots) and the fitted sigmoid function provided by Eq. 3 (red line) obtained from the FBP reconstruction. The FWHM of the Gaussian function obtained by computing the derivative of the fitting function was used as edge quality metric. (For interpretation of the references to colour in this figure legend, the reader is referred to the web version of this article.)

Table 1
Results of the edge quality measurements applied to a selected CT reconstruction slice of the CCFE11 mock-up by means of FBP, SIRT, SART, and CGLS reconstruction algorithms.

CTrec.algorithm	FWHM (pixels)	$\sigma_{(FWHM)}$ (pixels)
FBP	11.1608	0.4562
SIRT	11.3471	0.3961
SART	11.8307	0.7725
CGLS	10.6308	0.4070

hence the Full Width at Half Maximum (FWHM) and its standard deviation were evaluated from the parameter p_1:

$$FWHM = \frac{2\sqrt{ln2}}{p_1}, \qquad \sigma_{FWHM} = \frac{2\sqrt{ln2}}{p_1^2}\sigma_{p_1}. \qquad (6)$$

The FWHM values were used to assess the edge quality quantitatively and a lower FWHM values indicate sharper edges.

In Fig. 6 we have shown a comparison of a reconstructed slice for the CCFE11 mock-up carried out with all the CT reconstruction algorithms mentioned before. The panels in this figure refer to the same cross sectional slice within the specimen for direct comparison.

The pixel values histogram, represented below each image, has a multimodal and overall very similar behaviour for the different CT reconstruction algorithms. We note from a visual inspection that the image quality of the SART reconstruction is poorer compared to the

others. Different parameters were applied to improve its features but without any significant change. In terms of the quality indexing, reported in the upper part of every image, the SIRT method outperforms the other CT reconstructions in term of CNR value, whereas the CGLS method has produced better results for the SSIM and NRMSE indexes. From the edge quality prospective, the resulting edge spread function ESF obtained by averaging 20 line profiles traced across the Tungsten edge within the ROI (right panel of Fig. 5) is shown in Fig. 7 for the FBP reconstruction case.

The Full Width at Half Maximum (FWHM) of the Gaussian function obtained by computing the derivative of the sigmoid fitting function and described before (superimposed as a red solid line to the experimental ESF), was used as edge quality metric and reported for all the different CT reconstruction methods in Table 1.

Superior edge quality was registered for the CGLS reconstruction, proving that this algorithm outperforms, three out of four, image quality metrics of the other reconstruction methods. As such, the CGLS reconstruction algorithm was used in the rest of this work. A post-process denoising filter was applied to the CT reconstructed image to further improve its CNR but without compromising its overall quality. In fact, a higher CNR could help simplify and improve the segmentation in the following steps of the data analysis. We have considered as a reference image, labelled as "No denoise", the reconstructed slice obtained by the CGLS method. The post-process denoising filters considered in this study are: median filter, Gaussian filter, Block-matching and 3D filter (BM3D), and Non-Local Means filter (NLM) [36].
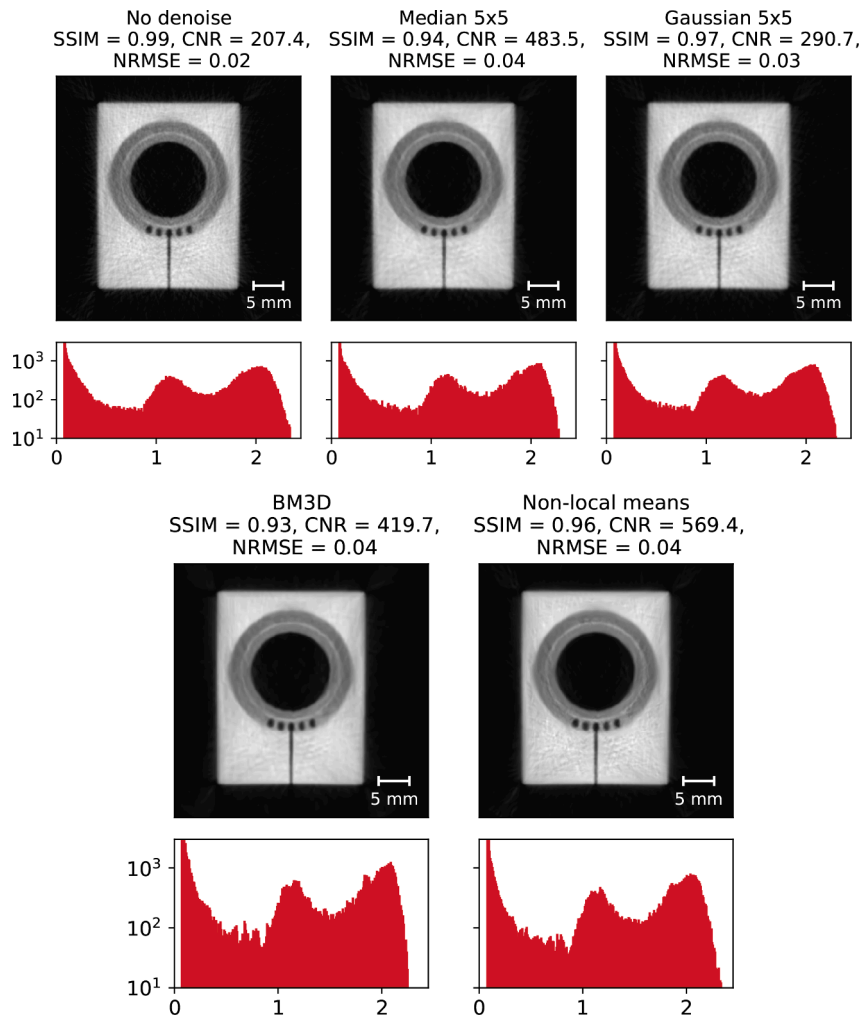

Fig. 8. Comparison of a post-processed CGLS reconstruction image filtered by means of median filter, Gaussian filter, BM3D and NLM denoising filters. Below each image, the grey value histogram is represented in the range $[0, 2.45]$ cm^{-1}.

Table 2
Results of the edge quality measurements applied to a selected CGLS reconstruction slice of the CCFE11 mock-up after application of median filter, Gaussian filter, BM3D and NLM denoising filters along with its relevant parameters. FWHM and $\sigma_{(FWHM)}$ are reported in pixels.

Filter type	parameters	FWHM	$\sigma_{(FWHM)}$
No denoise	none	10.6308	0.4070
Median	kernel size = 5	11.2994	0.6153
Gaussian	kernel size=5 σ computed from kernel size	11.0471	0.4430
BM3D	templateWindowSize=8 searchWindowSize=32 blockMatchingStep1=2500 blockMatchingStep2=400 groupSize=8, slidingStep=3 beta=2.7f	10.8442	0.5039
NLM	window size=21, patch size=11, h=3	10.7198	0.4576

The denoised images referring to the same slice within the specimen for direct comparison are displayed in Fig. 8. Their pixel values histogram, represented below each image, has a similar multimodal behaviour as observed in Fig. 6 with a slightly different width and intensity under each peak. An improved CNR was registered for all the filters applied but at the expense of a lower value for the other two quality indexes when compare to the reference image as reported in the upper part of any image. The Gaussian filter has produced better values in term of SSIM and NRMSE indexes, whereas the non-local means denoising filter outperform the others with the higher CNR and a better edge quality value as reported in Table 2, with the parameters employed for each filter listed as well for completeness.

Although both Gaussian and non-local means filters outperform the other denoise methods for two out of four metrics, the non-local means was chosen as a post-process filter for the rest of this work due to its higher CNR and superior edge quality.

4. Results and discussion

In this section we will discuss results showing volumetric defects present in the DEMO divertor mock-ups as illustrated above caused by manufacturing processes and/or generated by high heat flux loads. All the specimens were studied non-destructively with a minimum detectable defect size of 206 μm which is twice the pixel size used in the experimental setup according to the Niquist-Shannon sampling theorem [19]. Smaller defect sizes were considered to not be distinguishable with the current experimental setup that has been evaluated as the best compromise between the limited 30 s camera exposure time, i.e. the counting statistics, and the signal to noise ratio achieved in the tomography projections.

A reduction of the pipe wall thickness has been measured on one side of the CCFE11 mock-up above and below the top and bottom mono-blocks (as shown in the left panel of Fig. 9). Quantification of the thickness reduction was performed by means of comparing of line profiles located in the defect region (red line) and far from this location (blue line). The relative profiles are depicted in the right panel of Fig. 9 along with the results of the best fit by a rectangular-based function [37]. The full width at half maximum (FWHM) values, calculated by means of the distance of the centroids in the rise and fall edges of this function, were of 1.284 ± 0.016 mm and 1.603 ± 0.014 meaning a 19.9% reduction of the pipe wall thickness in the defect area with respect to its nominal value of 1.6 mm according to design specifications. It can be noted that there is good agreement between the FWHM value computed in the region free of the defect (blue line profile) and its
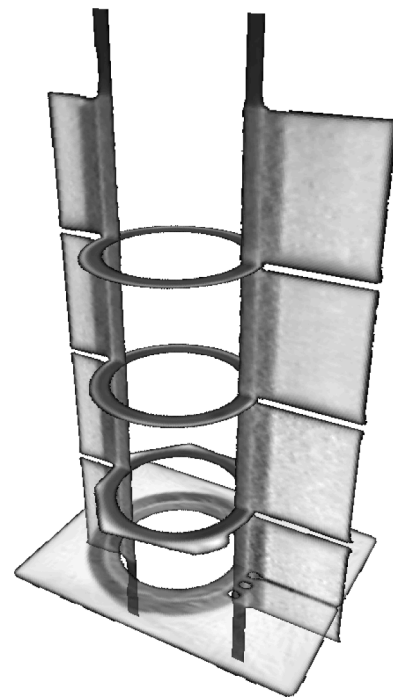

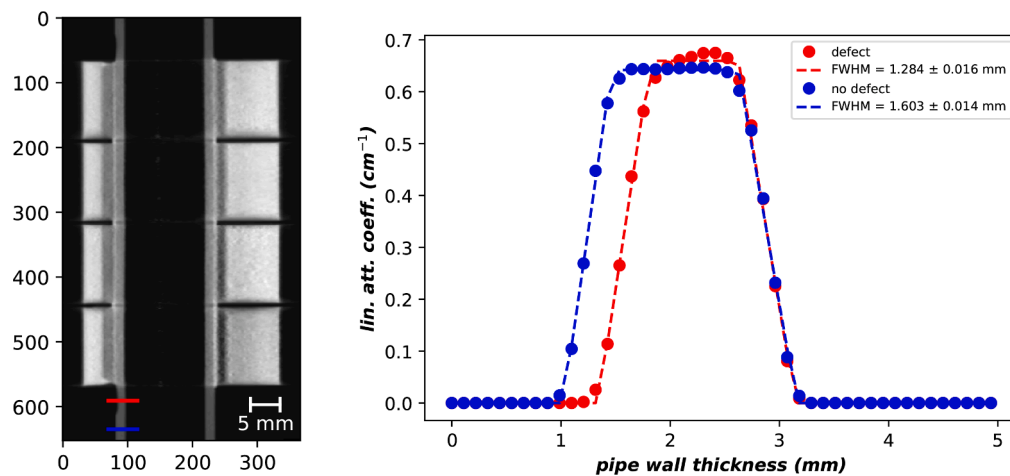**Fig. 10.** Ortho-view rendering of CCFE11 mock-up.

Fig. 9. (Left panel) Cross-section image of the pipe wall reduction on CCFE11 mock-up. Locations of the line profiles across the defect region (red line) and away from it (blue line). (Right panel) Relative intensity profiles for the highlighted ROI along with the results of the best fit. (For interpretation of the references to colour in this figure legend, the reader is referred to the web version of this article.)
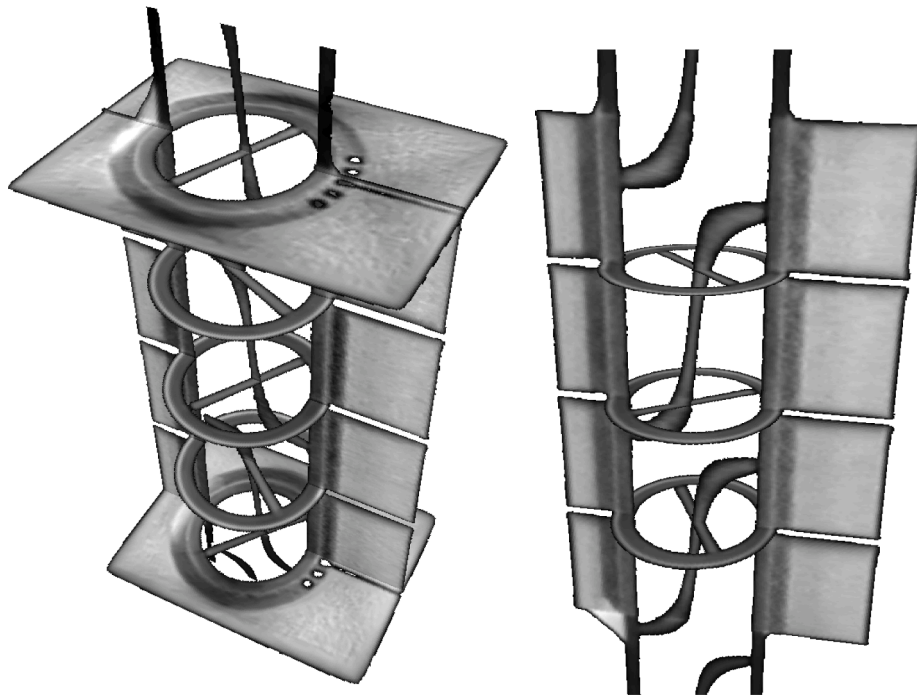
Fig. 11. Ortho-view rendering of CCFE9 (left panel) and CCFE10 (right panel) DEMO divertor target mock-ups.
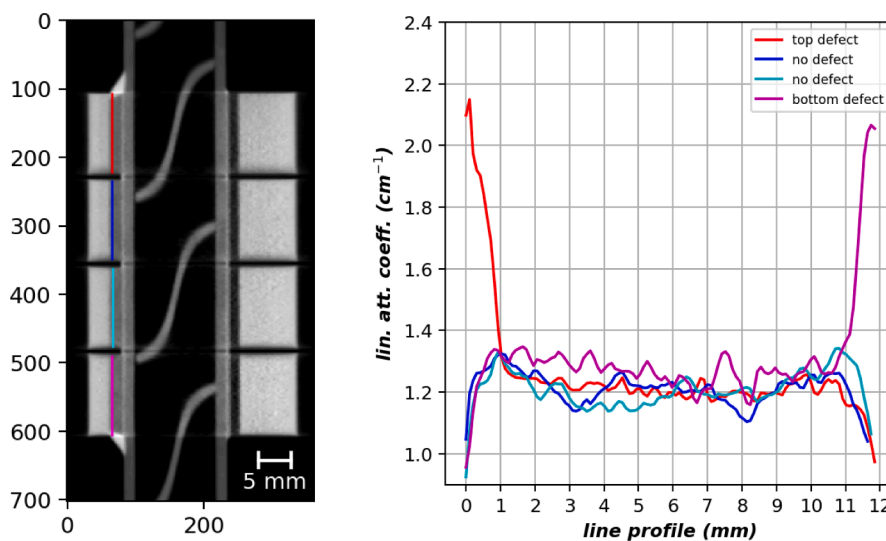

Fig. 12. (Left panel) Cross-section image highlighting spillover of some brazing materials in the CCFE9 mock-up. Locations of the line profiles in each monoblocks used for the quantification of its penetration depth. (Right panel) Relative intensity profiles for the highlighted line profile locations.

nominal pipe wall thickness value of 1.6 mm.

The inspection of all the reconstructed cross-section slices of the specimen has further allowed identification of an abnormal junction between two adjacent monoblocks as shown in the ortho-view rendering representation of the sample in Fig. 10. Here, the brazing material has partially filled the poor quality wire machining left in the OFHC copper layer resulting in an irregular shape of this junction if compared with the others visible in the same figure. Such a problem was not present for the other investigated mock-ups shown by the same ortho-view rendering format in Fig. 11. Instead, the three-dimensional map of the reconstructed linear attenuation coefficient values measured for CCFE9 and CCFE10 mock-ups (Fig. 11) have highlighted a spillover of some brazing material into the OFHC copper layer and outside the top and bottom monoblocks of the divertor targets.

In fact, brighter grey values attributable to the highly attenuating brazing material are clearly visible in the copper interlayer of these components (Fig. 11), and they extend deeply into this material as reported also in the cross-section views of the two specimens in the left panels of Figs. 12 and 13. Quantitative evaluations of the penetration depth of such brazing alloys into the copper interlayer has been obtained by analysis of four different line profiles localised in each monoblock of the sample as reported in the left panel of Figs. 12 and 13. The intensity profiles shown in the right panel of the same Figures have been colour coded for easier identification. It immediately leaps to the eye the different behaviour of the red and magenta intensity spectra belonging to the CCFE9 mock-up (see Fig. 12) compared to the cyan and blue line profiles. In the proximity of the brazing material they register a high value for the linear attenuation coefficient of 2.2 cm^{-1} that gradually
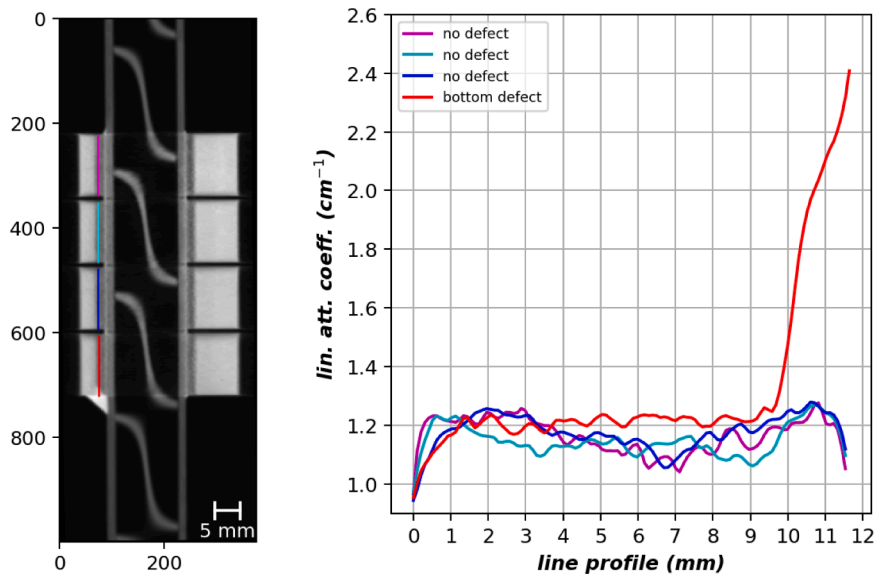
Fig. 13. (Left panel) Cross-section image highlighting spillover of some brazing materials in the CCFE10 mock-up. Locations of the line profiles in each monoblocks used for the quantification of its penetration depth. (Right panel) Relative intensity profiles for the highlighted line profile locations.
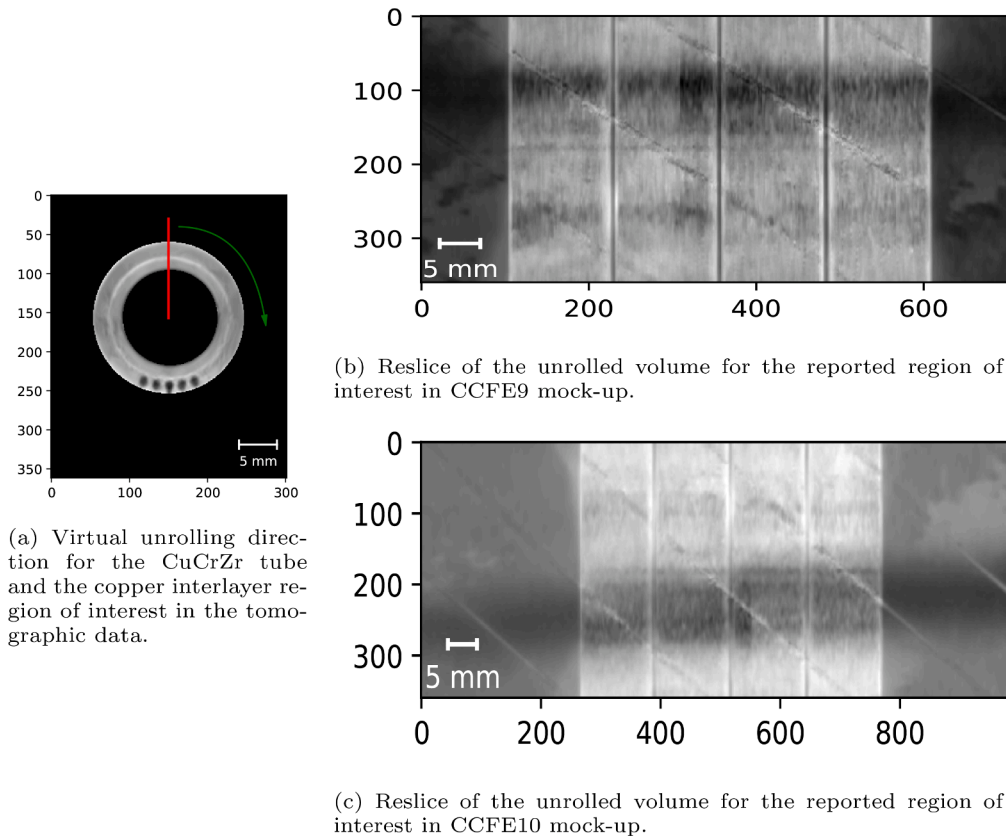

(a) Virtual unrolling direction for the CuCrZr tube and the copper interlayer region of interest in the tomographic data.

(b) Reslice of the unrolled volume for the reported region of interest in CCFE9 mock-up.

(c) Reslice of the unrolled volume for the reported region of interest in CCFE10 mock-up.

Fig. 14. Radial reslice orientation and marks on the CuCrZr pipe.

decreases inside the copper material to its nominal value of about 1.3 cm^{-1}. This can be interpreted as a gradual decrease in the fraction of brazing material depending on the penetration depth into the copper interlayer. It can be speculated that the maximum penetration depth reached by the brazing alloys was about 1 mm for both the top and bottom monoblocks. A similar conclusion can be drawn for the CCFE10 mock-up (see Fig. 13) where the bottom monoblock has experienced a similar infiltration of brazing alloys into the depth of copper interlayer

for about 1.5 mm. No sign of pipe wall thickness reduction has been observed for these two mock-ups.

CCFE9 and CCFE10 mock-ups differ from the CCFE11 mock-up by the presence of an internal helical swirl tape in the CuCrZr tube used to generate swirl-induced heat transfer enhancement. However, the impact of its use on a divertor target needs to be carefully studied to avoid undesired damage to the CuCrZr pipe. We approached the search for defects created by the use of the swirl tape by means of virtual unrolling
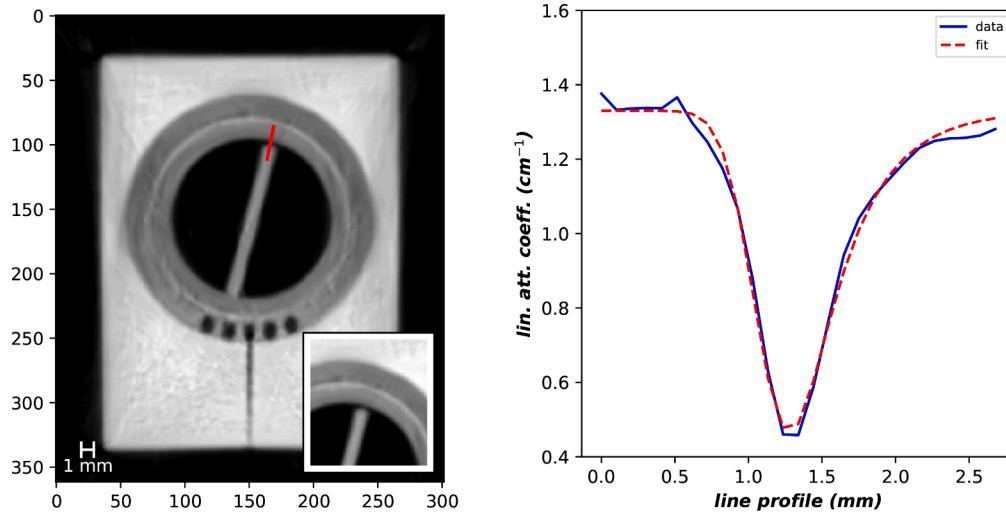
Fig. 15. Example of the gap between the swirl tape with the pipe's internal surface for the CCFE9 mock-up.

techniques of tomographic data in a region of interest that included only the CuCrZr tube and the OFHC interlayer as shown in Fig. 14a. The selected direction of unrolling is clockwise as highlighted by the green arrow in Fig. 14a.

The resliced unrolled volumes of CCFE9 and CCFE10 are given in Fig. 14b and c, respectively. In both divertor targets regular oblique lines are visible. The inclination of these marks is compatible with the imprinting left by the stainless steel swirl tape on the pipe's internal surface. These results confirm similar observations reported in a recent study performed on a different DEMO divertor mock-up based on ultrasonic testing methods [38]. The scratches are attributed to the higher hardness of steel compared to copper and the expansion due to water temperature or by vibrations that induced fretting of the swirl tape on the tube surface.

Although the marks left on the CuCrZr pipe testify a good overall adhesion of the tape to the surface thus ensuring the intended flow of cooling water, this is not enough to demonstrate that it is true along the entire length of the tube. The benefit of using neutron tomography is its capability to inspect a component virtually, slice-by-slice, throughout the entire volume with an inter-planar distance between each slice of about the pixel size, i.e. 103 μm. This has allowed the identification of some locations where the swirl tape is not in contact with the pipe's internal surface as shown in Fig. 15.

The gap between the tape and the pipe is visible in the data by the naked eye and shown better in the zoom view reported in the insert of the figure. Quantification of the distance across these two components can be addressed by analysis of the line profile drawn in red in the left panel of Fig. 15. The relative intensity profile, reported in the right panel can be fitted by means of an exponentially modified Gaussian distribution [37]. Results of the best fit were superimposed on the intensity data. The extension of the gap, extracted by the computed FWHM of the fitting function, is 0.440 ± 0.010 mm. This flaw could have a profound repercussion on the swirl-induced heat transfer enhancement enabled by the use of the swirl tape and potentially changing the water flow circulation in some unpredictable way. No major changes and additional damages were observed in the mockup subject to HHF loads. This could be a further confirmation of the good performance of this divertor design and its ability to withstand at high thermal loads like the ones expected for DEMO reactor. In principle, the digital volume of the mock-up reconstructed from the tomography scan allows to quantify such defects and therefore could offer a way forward to better understand the impact of these flaws. In fact, image-based simulation [39,40] could be used to calculate the change of the cooling water flow and eventually allows to predict more realistic performance parameters of the divertor target.

5. Conclusions

In this work we have demonstrated for the first time the feasibility of using neutron tomography to detect volumetric defects within DEMO divertor mock-ups with a spatial resolution of the order of hundreds of micrometers. Further improvements on detection of flaws down to several tens of micrometers is possible for divertor and other fusion components, and currently under investigation. All of the DEMO divertor mock-ups studied in this work have shown only a few manufacturing issues mainly connected with spill over of the brazing alloys that in some cases have infiltrated deeply into the copper interlayer. Virtual unrolling of tomographic data in a region of interest that has included the CuCrZr tube and OFHC interlayer has shown imprinting left by the stainless steel swirl tape on the pipe's internal surface. Furthermore, a poor contact between the swirl tape and the CuCrZr pipe has been measured along the length of the mock-ups. This issue could have repercussions on the swirl-induced heat transfer enhancement brought by the use of the tape and the potential change of water flow circulation in some unpredictable way. In principle, the digital tomography volume of the mock-up which includes such defects could offer a way forward to better understand and model the impact of these flaws on the performance of this component. In fact, image-based simulations could be used to predict the change of the cooling water flow and eventually allow more realistic performance parameters of the divertor target to be considered. Finally, this work has demonstrated that neutron tomography can produce valuable data for both the R&D cycle of fusion component design and inquality assurance of manufacturing if used appropriately.

Credit Author Statment

F.S., H.L., T.M. and LL.M.E. conceived the original idea. T.M, F.S. and LL.M.E. performed the neutron measurements at the IMAT beamline. T. M. carried out the data curation, formal analysis, validation and developed the analysis software. T.M. supervised the project, F.S. and H. L. worked on the funding acquisition for the project. T.M. wrote the manuscript and all authors reviewed it.

Declaration of Competing Interest

The authors declare that they have no known competing financial interests or personal relationships that could have appeared to influence the work reported in this paper.

Acknowledgements

References

[1] G. Federici, C. Skinner, J. Brooks, J. Coad, C. Grisolia, A. Haasz, A. Hassanein, V. Philipps, C. Pitcher, J. Roth, W. Wampler, D. Whyte, Plasma-material interactions in current tokamaks and their implications for next step fusion reactors, Nucl. Fusion 41 (12) (2001) 1967–2137, https://doi.org/10.1088/0029-5515/41/12/218.

[2] J. You, E. Visca, T. Barrett, B. Böswirth, F. Crescenzi, F. Domptail, M. Fursdon, F. Gallay, B.-E. Ghidersa, H. Greuner, M. Li, A. Müller, J. Reiser, M. Richou, S. Roccella, C. Vorpahl, European divertor target concepts for demo: design rationales and high heat flux performance, Nucl. Mater. Energy 16 (2018) 1–11, https://doi.org/10.1016/j.nme.2018.05.012.

[3] J. You, E. Visca, T. Barrett, B. Böswirth, F. Crescenzi, F. Domptail, G. Dose, M. Fursdon, F. Gallay, H. Greuner, K. Hunger, A. Lukenskas, A. Müller, M. Richou, S. Roccella, C. Vorpahl, K. Zhang, High-heat-flux technologies for the european demo divertor targets: state-of-the-art and a review of the latest testing campaign, J. Nucl. Mater. 544 (2021) 152670, https://doi.org/10.1016/j.jnucmat.2020.152670.

[4] F. Romanelli, Fusion Electricity, A Roadmap to the Realization of Fusion Energy, European Fusion Development Agreement. Technical Report, EFDA, 2012.

[5] C. Pei, H. Liu, J. Qiu, T. Liu, Z. Chen, Progress on the ultrasonic testing and laser thermography techniques for NDT of tokamak plasma-facing components, Theor. Appl. Mech. Lett. 9 (3) (2019) 180–187, https://doi.org/10.1016/j.taml.2019.03.011.

[6] M. Merola, P. Chappuis, F. Escourbiac, M. Grattarola, H. Jeskanen, P. Kauppinen, L. Plöchl, B. Schedler, J. Schlosser, I. Smid, S. Tähtinen, R. Vesprini, E. Visca, A. Zabernig, Non-destructive testing of divertor components, Fusion Eng. Des. 61–62 (2002) 141–146, https://doi.org/10.1016/S0920-3796(02)00155-2.

[7] S. Roccella, E. Cacciotti, F. Escourbiac, A. Pizzuto, B. Riccardi, A. Tatì, P. Varone, E. Visca, Development of an ultrasonic test method for the non-destructive examination of iter divertor components, Fusion Eng. Des. 84 (7–11) (2009) 1639–1644, https://doi.org/10.1016/j.fusengdes.2008.12.096.

[8] S. Roccella, E. Cacciotti, D. Candura, A. Mancini, A. Pizzuto, A. Reale, A. Tatí, E. Visca, Ultrasonic test of carbon composite/copper joints in the iter divertor, Fusion Eng. Des. 88 (9) (2013) 1802–1807, https://doi.org/10.1016/j.fusengdes.2013.05.078.

[9] S. Roccella, A. Reale, A. Tatí, E. Visca, M. Palermo, P. Gavila, Enea ultrasonic test on plasma facing units, Fusion Eng. Des. 146 (2019) 2356–2360, https://doi.org/10.1016/j.fusengdes.2019.03.189.

[10] L. Evans, T. Minniti, M. Fursdon, M. Gorley, T. Barrett, F. Domptail, E. Surrey, W. Kockelmann, A. v. Müller, F. Escourbiac, A. Durocher, Comparison of x-ray and neutron tomographic imaging to qualify manufacturing of a fusion divertor tungsten monoblock, Fusion Eng. Des. 134 (2018) 97–108, https://doi.org/10.1016/j.fusengdes.2018.06.017.

[11] J. You, G. Mazzone, E. Visca, C. Bachmann, E. Autissier, T. Barrett, V. Cocilovo, F. Crescenzi, P. Domalapally, D. Dongiovanni, S. Entler, G. Federici, P. Frosi, M. Fursdon, H. Greuner, D. Hancock, D. Marzullo, S. McIntosh, A. Müller, M. Porfiri, G. Ramogida, J. Reiser, M. Richou, M. Rieth, A. Rydzy, R. Villari, V. Widak, Conceptual design studies for the european demo divertor: rationale and first results, Fusion Eng. Des. 109–111 (2016) 1598–1603, https://doi.org/10.1016/j.fusengdes.2015.11.012.

[12] T. Barrett, S. McIntosh, M. Fursdon, D. Hancock, W. Timmis, M. Coleman, M. Rieth, J. Reiser, Enhancing the demo divertor target by interlayer engineering, Fusion Eng. Des. 98–99 (2015) 1216–1220, https://doi.org/10.1016/j.fusengdes.2015.03.031.

[13] M. Fursdon, T. Barrett, F. Domptail, L.M. Evans, N. Luzginova, N.H. Greuner, J.-H. You, M. Li, M. Richou, F. Gallay, E. Visca, The development and testing of the thermal break divertor monoblock target design delivering 20 MW m-2 heat load capability, Phys. Scr. T170 (2017) 014042, https://doi.org/10.1088/1402-4896/aa8c8e.

[14] A. Lukenskas, T. Barrett, M. Fursdon, F. Schoofs, H. Greuner, G. Dose, S. Roccella, E. Visca, F. Gallay, M. Richou, J.-H. You, High heat flux test results for a thermal break demo divertor target and subsequent design and manufacture development, Fusion Eng. Des. 146 (2019) 1657–1660, https://doi.org/10.1016/j.fusengdes.2019.03.010.

[15] H. Greuner, B. Böswirth, T. Barrett, F. Crescenzi, F. Gallay, K. Hunger, M. Richou, E. Visca, A. von Müller, J. You, Progress in high heat flux testing of european demo divertor mock-ups, Fusion Eng. Des. 146 (2019) 216–219, https://doi.org/10.1016/j.fusengdes.2018.12.021.

[16] M. Strobl, I. Manke, N. Kardjilov, A. Hilger, M. Dawson, J. Banhart, Advances in neutron radiography and tomography, J. Phys. D 42 (24) (2009) 243001, https://doi.org/10.1088/0022-3727/42/24/243001.

[17] H.Z. Bilheux, R. McGreevy, I.S. Anderson, Neutron Imaging and Applications, Springer, Boston, 2009.

[18] N. Kardjilov, I. Manke, R. Woracek, A. Hilger, J. Banhart, Advances in neutron imaging, Mater. Today 21 (6) (2018) 652–672, https://doi.org/10.1016/j.mattod.2018.03.001.

[19] A.C. Kak, M. Slaney, G. Wang, Principles of computerized tomographic imaging, Med. Phys. 29 (1) (2002), https://doi.org/10.1118/1.1455742.107–107

[20] T. Minniti, W. Kockelmann, G. Burca, J. Kelleher, S. Kabra, S. Zhang, D. Pooley, E. Schooneveld, Q. Mutamba, J. Sykora, N. Rhodes, F. Pouzols, J. Nightingale, F. Aliotta, L. Bonaccorsi, R. Ponterio, G. Salvato, S. Trusso, C. Vasi, A. Tremsin, G. Gorini, Materials analysis opportunities on the new neutron imaging facility IMAT@ISIS, J. Instrum. 11 (03) (2016), https://doi.org/10.1088/1748-0221/11/03/c03014.C03014–C03014

[21] W. Kockelmann, G. Burca, J.F. Kelleher, S. Kabra, S.-Y. Zhang, N.J. Rhodes, E. M. Schooneveld, J. Sykora, D.E. Pooley, J.B. Nightingale, F. Aliotta, R.C. Ponterio, G. Salvato, D. Tresoldi, C. Vasi, J.B. McPhate, A.S. Tremsin, Status of the neutron imaging and diffraction instrument IMAT, Phys Procedia 69 (2015) 71–78, https://doi.org/10.1016/j.phpro.2015.07.010.

[22] T. Minniti, K. Watanabe, G. Burca, D.E. Pooley, W. Kockelmann, Characterization of the new neutron imaging and materials science facility IMAT, Nucl. Instrum. Methods Phys. Res. Sect. A 888 (2018) 184–195, https://doi.org/10.1016/j.nima.2018.01.037.

[23] W. Kockelmann, T. Minniti, D.E. Pooley, G. Burca, R. Ramadhan, F.A. Akeroyd, G. D. Howells, C. Moreton-Smith, D.P. Keymer, J. Kelleher, S. Kabra, T.L. Lee, R. Ziesche, A. Reid, G. Vitucci, G. Gorini, D. Micieli, R.G. Agostino, V. Formoso, F. Aliotta, R. Ponterio, S. Trusso, G. Salvato, C. Vasi, F. Grazzi, K. Watanabe, J.W. L. Lee, A.S. Tremsin, J.B. McPhate, D. Nixon, N. Draper, W. Halcrow, J. Nightingale, Time-of-flight neutron imaging on IMAT@ISIS: a new user facility for materials science, J. Imaging 4 (3) (2018), https://doi.org/10.3390/jimaging4030047.

[24] D. Micieli, T. Minniti, G. Gorini, Neutompy toolbox, a python package for tomographic data processing and reconstruction, SoftwareX 9 (2019) 260–264, https://doi.org/10.1016/j.softx.2019.01.005.

[25] Amira-Avizo Software website, url = https://www.thermofisher.com/uk/en/home/industrial/electron-microscopy/electron-microscopy-instruments/workflow-solutions/3d-visualization-analysis-software.html.

[26] I. Antcheva, M. Ballintijn, B. Bellenot, M. Biskup, R. Brun, N. Buncic, P. Canal, D. Casadei, O. Couet, V. Fine, L. Franco, G. Ganis, A. Gheata, D.G. Maline, M. Goto, J. Iwaszkiewicz, A. Kreshuk, D.M. Segura, R. Maunder, L. Moneta, A. Naumann, E. Offermann, V. Onuchin, S. Panacek, F. Rademakers, P. Russo, M. Tadel, ROOT-A C++ framework for petabyte data storage, statistical analysis and visualization, Comput. Phys. Commun. 180 (12) (2009) 2499–2512, https://doi.org/10.1016/j.cpc.2009.08.005.

[27] C.A. Schneider, K.W. Eliceiri, NIH image to imagej: 25 years of image analysis, Nat. Methods 9 (2012) 671–675, https://doi.org/10.1038/nmeth.2089.

[28] A.P. Kaestner, MuhRec-a new tomography reconstructor, Nucl. Instrum. Methods Phys. Res. Sect. A 651 (1) (2011) 156–160, https://doi.org/10.1016/j.nima.2011.01.129.

[29] B. Münch, P. Trtik, F. Marone, M. Stampanoni, Stripe and ring artifact removal with combined wavelet – Fourier filtering, Opt. Express 17 (10) (2009) 8567–8591, https://doi.org/10.1364/OE.17.008567.

[30] P. Gilbert, Iterative methods for the three-dimensional reconstruction of an object from projections, J. Theor. Biol. 36 (1) (1972) 105–117, https://doi.org/10.1016/0022-5193(72)90180-4.

[31] A.H. Andersen, A.C. Kak, Simultaneous algebraic reconstruction technique (SART): a superior implementation of the art algorithm, Ultrason Imaging 6 (1) (1984) 81–94, https://doi.org/10.1177/016173468400600107.

[32] J.A. Scales, Tomographic inversion via the conjugate gradient method, Geophysics 52 (2) (1987) 179–185, https://doi.org/10.1190/1.1442293.

[33] Zhou Wang, A.C. Bovik, H.R. Sheikh, E.P. Simoncelli, Image quality assessment: from error visibility to structural similarity, IEEE Trans. Image Process. 13 (4) (2004) 600–612, https://doi.org/10.1109/TIP.2003.819861.

[34] D. Micieli, T. Minniti, V. Formoso, W. Kockelmann, G. Gorini, A comparative study of reconstruction methods applied to neutron tomography, J. Instrum. 13 (06) (2018), https://doi.org/10.1088/1748-0221/13/06/c06006.C06006–C06006

[35] D. Micieli, T. Minniti, L.M. Evans, G. Gorini, Accelerating neutron tomography experiments through artificial neural network based reconstruction, Sci. Rep. 9 (1) (2019) 2450, https://doi.org/10.1038/s41598-019-38903-1.

[36] R. Szeliski, Computer Vision Algorithms and Applications, first ed., Springer-Verlag London, 2011 https://doi.org/10.1007/978-1-84882-935-0.

[37] LMFIT, non-linear least-squares minimization and curve-fitting for Python, url = https://lmfit.github.io/lmfit-py/builtin_models.html#builtin-models-chapter.html.

[38] S. Roccella, G. Dose, T. Barrett, E. Cacciotti, L. Dupont, F. Gallay, H. Greuner, M. Richou, A. Tatí, E. Visca, J.-H. You, Ultrasonic test results before and after high

heat flux testing on w-monoblock mock-ups of eu-demo vertical target, Fusion Eng. Des. 160 (2020) 111886, https://doi.org/10.1016/j.fusengdes.2020.111886.

[39] L. Evans, T. Minniti, T. Barrett, A.V. Muller, L. Margetts, Virtual qualification of novel heat exchanger components with the image-based finite element method, NDT-net 2019-03 (2019) 1–10.

[40] L. Evans, L. Margetts, V. Casalegno, L. Lever, J. Bushell, T. Lowe, A. Wallwork, P. Young, A. Lindemann, M. Schmidt, P. Mummery, Transient thermal finite element analysis of CFC–Cu ITER monoblock using x-ray tomography data, Fusion Eng. Des. 100 (2015) 100–111, https://doi.org/10.1016/j.fusengdes.2015.04.048.